Measurement of attractive interactions produced by the ion wakefield in dusty plasmas using a constrained collision geometry

G. A. Hebner and M. E. Riley
Sandia National Laboratories, Albuquerque, New Mexico 87185-1423, USA
(Received 28 April 2003; published 2 October 2003)

Plasma dust particle interactions, charges, and screening lengths are derived from measurements of time-dependent particle positions in a simplified geometry. The magnitude and structure of the ion wakefield potential below a negatively charged dust particle levitated in the plasma sheath region were measured as functions of the pressure and interparticle spacing. Attractive and repulsive components of the interaction force were extracted from a trajectory analysis of low-energy dust collisions between different mass particles in a well-defined electrostatic potential that constrained the dynamics of the collisions to be one-dimensional. Typical peak attractions varied between 60 and 230 fN while the peak particle-particle repulsion was on the order of 60 fN. Random thermal motion of the particles contributed to observable rates for transitions between different equilibrium configurations of vertically separated particles. The influence of nearest- and non-nearest-neighbor interactions on calculated particle parameters is examined using several methods.

DOI: 10.1103/PhysRevE.68.046401 PACS number(s): 52.27.Lw, 52.27.Gr

I. INTRODUCTION

Dust is a component of plasmas as diverse as interstellar regions, planetary rings, fusion reactors, and laboratory microelectronics processing systems. In such tightly coupled dust-plasma systems, the dust modifies the plasma properties and the plasma gives rise to a number of long-range and collective interactions between the dust particles. Particle-particle interactions and the forces that drive the interactions depend on a myriad of variables such as plasma characteristics, dust density and material, external potentials, and the flow of plasma past the particles. For micron-sized dust particles immersed in idealized, isotropic plasmas, the particle interaction is well represented by a repulsive, screened Coulomb interaction. However, in most realistic systems, there is a positive ion flow around the negatively charged particles which warps the sheath structure around the particles and generates a wakefield or a net positive space-charge region downstream from the particle due to ion focusing [1–4]. This positive space-charge region interacts with the negatively charged particles to give rise to an attractive interaction and a number of collective interactions in dusty plasmas.

It is well known that dust particles levitated at the plasma sheath can form single-layer [two-dimensional (2D)] hexagonal-close-packed, triangular lattice structures that are dominated by repulsive screened Coulomb (Debye) interaction [5–8]. More complicated 3D assemblies in dusty plasmas show a range of order from face- and body-centered-cubic lattices to more amorphous arrangements [9–12]. In the simplest view, the stability of multilayer structures appears to depend on the delicate balance between an attractive ion wakefield potential and repulsive Debye potentials [9,13]. However, this simple view is not universally accepted because the largest 3D dust arrangements apparently show little wakefield effect [14]. Thus the full impact of the attractive interaction on dusty plasma collective interactions appears to an open question. In large part, this is due to the lack of measurements of the magnitude of the effect and its scaling with plasma conditions. In most terrestrial dusty plasma systems, the ion wakefield dimensions are on the order of the plasma Debye length (50–500 μm) and usual probe techniques are not possible.

Several recent measurements have begun to address this issue. Melzer and co-workers recently observed a nonreciprocal attractive interaction between two different mass particles [15,16]. They measured an attractive force on the order of 1–8 fN for a helium plasma and dust particles considerably smaller than those used here. Their technique used a laser to push the particles a small distance away from the minimum of the attractive potential well. From an analysis of the particle trajectories after the laser is turned off, during which time the particles relax back to an equilibrium position, a portion of the attractive potential well can be determined. We recently measured peak attractive interactions in 100 mTorr argon plasmas that were on the order of 200 fN [17]. Our technique determines the shape of the entire attractive and repulsive potential from an analysis of constrained 1D collisions between particles that originate at far distances from each other. The dust particles themselves were used as probes of the wakefield potential. This work expands on our previous study and examines changes in both the magnitude and shape of the ion-wakefield-induced attractive potential with pressure and vertical particle spacing. In addition, the magnitude and shape of the particle-particle repulsive potential is derived.

We have also used the present geometry to measure the charge Z on the particles and the screening length λ using a compressional or equation-of-state (EOS) analysis. These two quantities are fundamental parameters that depend on the electron density, electron temperature, particle characteristics, and plasma sheath characteristics. In prior work, λ has been determined from Langmuir probe measurements of plasma properties [18,19] or laser excitation of horizontal waves in the dust crystal [20]. Measurements of Z have relied on laser and rf excited resonance techniques [21] and models of the electrode sheath [22]. In contrast with prior work, our analysis does not rely on measurements of the

plasma parameters and/or analytic models of the plasma sheath. However, our analysis does rely on a model for the particle interaction potential (screened Coulomb) that is supported by measurements [8] and, in the case of 2D dusty plasmas, compares well with resonance techniques [6]. Using the present simplified geometry, we present two methods to derive Z and λ values and then examine the uncertainty introduced by neglecting non-nearest-neighbor interactions for linear particle arrangements.

To reduce ''potential'' confusion, we mention that there are two potential wells that are discussed during the course of this work. The first is the potential well formed by the structure of the lower electrode and the rf driven sheath that forms above it. It is within this externally imposed potential well that all the particles move and collide. The second, the ion wakefield potential well, is the electrical potential formed downstream of each individual particle by the positive ion flow. This potential well is responsible for nonreciprocal particle-particle attraction investigated in this work.

II. EXPERIMENTAL SETUP

Particle interaction potentials, charge, and screening lengths are derived from measurements of the particle interactions in a simplified geometry. The experiments were performed in an asymmetrically driven, parallel plate discharge chamber, a modified gaseous electronics conference (GEC) rf reference cell [23]. The lower electrode was capacitively coupled and driven at 20 MHz and 1.8 W. Electron density was approximately 5×10^{8} cm^{-3} while electron temperature was 3 eV, as determined by a Langmuir double probe [6]. No external magnetic field was applied. Argon gas flow was 2 sccm at 60 and 100 mTorr. The 10-cm-diam lower electrode contained a 5-cm-diam insert that was machined with a 0.5 m radius of curvature spherical shape [5,17]. Following this slight curvature, we machined a slot 3 mm wide and 2 mm deep across the diameter of the insert. A not-to-scale sketch of the rf-driven electrode and slot is shown in Fig. 1. The particles were illuminated by a 532 nm, 10 mW laser using a sheet of light produced with a scanning mirror and cylindrical lens. Top and side views of the time-dependent particle trajectories were captured on videotape using two CCD cameras and lenses. Pixel resolution was approximately 0.015 mm. The videotape was digitized frame by frame and the particle position extracted using image analysis algorithms. The time spacing was 30 frames/s.

Dust particles released above the plasma quickly develop a negative charge, and fall downward under the influence of gravity and viscosity until the force of gravity is balanced by the time-averaged sheath electric field produced by the lower rf-driven electrode. A schematic representation of such an electrical equipotential surface is shown in Fig. 1, as is the location of the particles trapped in this potential well. Once confined to the surface by the time-average electric field, the particles move mostly horizontally under the influence of gravity to lower-energy locations (color variations depict height of the surface). The electrode slot forms a steep potential gradient perpendicular to the line defined by the slot, with a curvature that is on the order of the plasma sheath

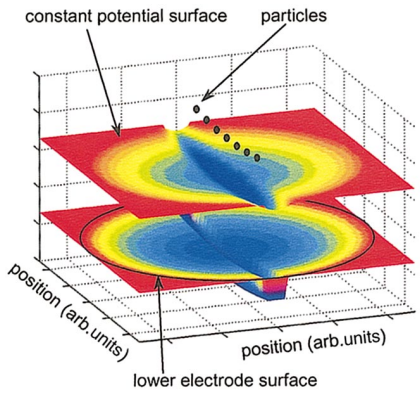

FIG. 1. (Color) Schematic of a portion of the experimental configuration showing the lower, rf-driven electrode, a constant potential surface, and the location of the linear particle assembly. The color contours in the lower electrode surface encode height (in arbitrary units) and show the location of the 3-mm-wide by 2-mm-deep trench machined into a 0.5 m radius of curvature, 5-cm-diam lower electrode insert (marked by the black circle). An artist rendition of what a constant potential surface could look like is shown above the lower electrode. The entire surface has a constant, time-averaged electric field and the colors encode height (in arbitrary units). While the curvature of the constant potential surface can conform to the 0.5 m scale length, the finite plasma sheath will smooth out the trench structure. The particles align themselves on this surface where the gravitational energy in minimized, i.e., above the trench.

thickness, approximately 5 mm. For this work, only linear arrangements of particles are generated or considered. With this arrangement we could reproducibly generate collinear collisions with a constant vertical offset (impact parameter) using two particles of different mass. The vertical confining forces (electric sheath, gravity, and ion wind) are much stronger than the weak particle-particle interactions or random Brownian motion, resulting in collision dynamics constrained to motion in the coordinate axis parallel to the trough. The vertical movement of the injected particles damped quickly, as did any oscillation normal to the trough. In addition, the amplitude of Brownian motion normal to the trough was considerably less than the particle's distance of closest approach.

The electrostatic trench was used for two different experiments. The first used particles of the same mass, and hence the same height above the lower electrode, to generate the particle charge Z and plasma screening length λ from an analysis of the radially dependent particle spacing resulting from gravitational compression. For this experiment, a few (1–12) Melamine particles were dropped into one end of the trough using a shaker arrangement. The particles slid down the gravitational well until they formed a line of particles (Fig. 2). The photo shows 12 particles of the same diameter (mass) confined to a line by the electrostatic potential surface. For most conditions investigated, more than 12–14 particles resulted in kinked lines. The center of the arrangement is at the center of the potential well. Due to the 0.5 m radius of curvature of the lower electrode, the particle spacing in the center of the line is slightly smaller than at the edges. We

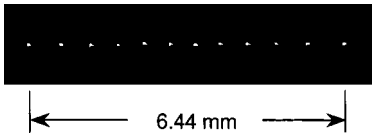

FIG. 2. Side view of a linear arrangement of twelve 11.9-μm-diam Melamine particles.

use this compression in a subsequent analysis to derive Z and λ.

The second set of experiments discussed in this paper examines the wakefield potential associated with an upper target dust particle by colliding it with a probe dust particle levitated at a lower height. For these measurements, a single Melamine particle was dropped into one end of the trough and fell to the bottom of the spherical electrode with a time constant determined by gas drag [5]. At a later time, a second particle with a different diameter, hence a different height above the lower electrode, was dropped into the opposite end of the trough. The resulting images as the particles collided at the bottom of the well were then recorded. The time-dependent particle positions were extracted from the digitized videotape and analyzed for the interaction force potentials. These two separate but complementary measurements are described in the following sections.

III. DETERMINATION OF Z AND λ

The charge Z on the particle and the screening length λ of the plasma sheath around each particle are fundamental parameters that depend on the particle and plasma characteristics. The linear arrangements of particles produced by our experimental geometry are a simplified system in which to test several methods of deriving Z and λ. In the following sections, we derive an equation-of-state description of the 1D particle arrangement. That analysis is compared with a direct method that sums the forces on the particles. The influence of including nearest-neighbor and non-nearest-neighbor interactions is discussed.

A. Equation of state for a 1D confined array of particles

In this section we derive a constitutive relation by means of an equation-of-state (EOS) analysis for the equilibrium assemblies of dust particles trapped in a linear array. Consider a single particle to be at equilibrium in the nearly vertical curvilinear coordinate perpendicular to the electrode. Because the ion wind and thermophoretic force vectors are perpendicular to the surface, we know that only gravity and the viscous forces can act to accelerate or decelerate an isolated particle in the lateral direction parallel to the trough. This allows us to write the r component of the force in a simplified form,

$$f_r = -h'(r)m_d g \approx -2cr m_d g \equiv -kr, \tag{1}$$

where $h(r) \approx cr^2$ is the height of the spherical surface of the lower electrode as one moves away, parallel to the trough, from the lowest position centered at $r=0$. The prime denotes a derivative, g is the acceleration due to gravity, and m_d is the mass of the dust particle. The constant $k = 2m_d g c = m_d g / R_c$ is a harmonic restoring force constant for the lateral motion about the center of the potential well if it is parabolic, and R_c is the radius of curvature of the lower electrode. We will treat the coordinate r like a Cartesian coordinate in the following discussion and allow $-\infty < r < \infty$.

We can simplify the analysis of the force balance between the repulsive pair interaction potential and the applied compressive force by deriving a continuum mechanics limit of the discrete particle array. Let $s(r)$ denote the nearest-neighbor (NN) spacing in the linear array, where the radius is written to acknowledge that the average spacing will vary within the array. The line number density is related to the NN spacing by

$$n = 1/s \tag{2}$$

at any point in the array.

We will take the pairwise interaction potential energy between the particles to be a function of the separation s of the particles, $V_{pair}(s)$. The potential energy per particle in a linear array is $V_{pair}(s)$ when NN interactions dominate. We will discuss corrections to the NN assumption below. The potential energy density within the layer is given by

$$e(r) = n(r) V_{pair}(s(r)), \tag{3}$$

which is in units of energy per distance in a 1D geometry.

From the steady-state Euler momentum equation for a continuum fluid, or just from simple addition of forces, one can argue that the equation relating the pressure $p(r)$ and external force applied to the array is just

$$\begin{aligned} \frac{dp(r)}{dr} &= n(r) f_r(r), \\ &= -n(r) m_d g h'(r), \\ &\approx -krn(r), \end{aligned} \tag{4}$$

where f_r is the force on an individual particle as given in Eq. (1).

Pressure is defined by the change in energy with volume, or with length in this 1D case. Consider a length L with N particles within L. The number density is $n = N/L$. Solving for p using Eq. (3) and the definitions of L, e, and n gives

$$\begin{aligned} p &= -\frac{dE}{dL} = -\frac{d[Le(s)]}{d[N/n(s)]} = -\frac{d[Ln(s)V_{pair}(s)]}{Nds} \\ &= -\frac{dV_{pair}(s)}{ds}. \end{aligned} \tag{5}$$

This relation applies at any position within the array where the local pressure is $p(r)$ and the NN separation is $s(r)$. However, it can only apply at the ends, $\pm r_M$, of the array, if the NN separation s is allowed to become infinite there. This is consistent with zero density for $r > x_M$. The appropriate boundary condition for the outer particle at the end of the

dust array can be found by balancing the inward force due to the external field with the pairwise force with the next inward particle. The force balance relation is

$$V'_{pair}(s_M) = f_r(r_M) \approx -kr_M, \tag{6}$$

for the positive end of the array, indicated by the use of the radial coordinate.

We can now combine Eqs. (4) and (5) to give a balance equation for the pressure within the array,

$$\frac{dp(r)}{dr} = -\frac{d}{dr}\frac{dV_{pair}(s)}{ds} = n(r) f_r(r), \tag{7}$$

in which s is implicitly a function of r. If we introduce Eq. (2) to replace the number density and the quadratic expression for the curvature implied in Eq. (1), this reduces to

$$sV''_{pair}(s)ds = krdr. \tag{8}$$

This is the equivalent of Eq. (21) in Ref. [6] for a linear array. The first integral of Eq. (8) can be found,

$$\left[s\frac{dV_{pair}(s)}{ds} - V_{pair}(s) \right]_{s_o}^{s} = \frac{1}{2}kr^2, \tag{9}$$

where the notation indicates that the expression is to be evaluated as $[f(x)]_a^b = f(b) - f(a)$. Boundary conditions have been applied such that $r=0$ corresponds to NN separation $s = s_o$ at the center of the array. As $s \to s_M$, where s_M is the maximum pairwise separation at the ends of the array, r approaches the outer radius (ends of the linear array) r_M. This expression for r_M is a function of s_o, reflecting the fact that the compression of the array at the center depends on the size and cumulative weight of the array. This can only be determined by an integration of the nonlinear ordinary differential Eq. (8) connecting r and s.

The goal of this work is to derive interaction parameters from observations of the plasma crystal compression. We do that by choosing the NN pair interaction to be a Debye-shielded Coulomb potential,

$$V_{pair}^{Debye}(r) = \frac{(q_d^2/4\pi\varepsilon_o)}{r}\exp(-r/\lambda) \equiv \frac{A}{r}\exp(-r/\lambda), \tag{10}$$

where q_d is the total charge on the particle $(-Ze)$ and λ is the screening length, the two parameters of interest. We note that no assumptions are made as to λ being the bulk plasma screening length. Evaluation of Eq. (9) gives

$$r^2(s) = \frac{2}{k}\left[\left(2 + \frac{s}{\lambda} \right) V_{pair}^{Debye}(s) \right]_{s}^{s_o} \tag{11}$$

using the same notation for the brackets as in Eq. (9). If we label the point in radius where the NN separation becomes infinite as r_∞, we see that r_∞ is given by

$$r_\infty^2 = \frac{2}{k}\left(2 + \frac{s_o}{\lambda} \right) V_{pair}^{Debye}(s_o). \tag{12}$$

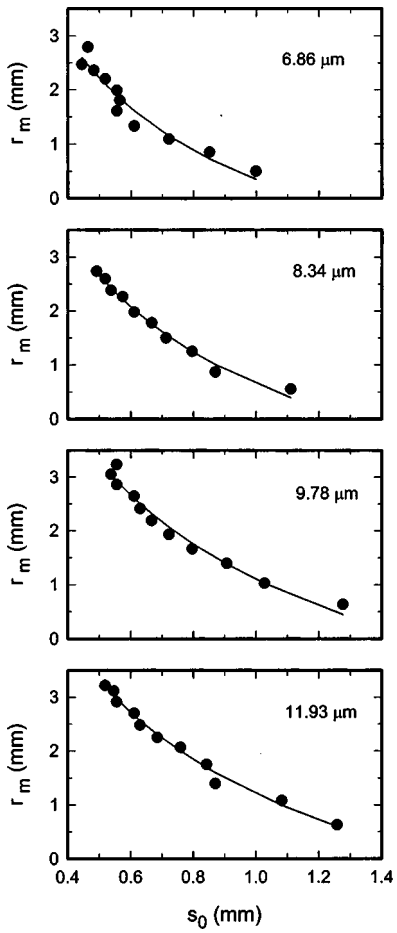

FIG. 3. Maximum radius of the linear particle assemblies as functions of the particle spacing in the center of the line for four different particle diameters. The line is a fit to the data using a 1D equation of state [Eq. (13)] to derive the charge on the particles and the screening length. The pressure was 100 mTorr.

The singular point r_∞ where $s \to \infty$ occurs at a point in radius greater than r_M. An approximate connection of r_∞ and r_M can be found to be $r_\infty \approx r_M + s_M/2$. This allows us to write down an equation suitable for determining Z and λ by a regression analysis (least-squares fitting) of data tabulating the minimum NN distance and maximum radius of the particle arrays,

$$r_M = -\frac{1}{2}s_o + \sqrt{\frac{2A}{k}\exp(-s_o/\lambda)\left(\frac{2}{s_o} + \frac{1}{\lambda} \right)}. \tag{13}$$

The constant A is defined in Eq. (10) and k in Eq. (1). The quantity s_M has been replaced by s_o in Eq. (13) without too much error in order to avoid unnecessary data tabulation. An example of the fits to Eq. (13) is shown in Fig. 3 for four different particle sizes. The charges on the dust particles were 7400, 10 400, 14 300, and 19 500 electrons, and the screening lengths were 270, 330, 410, and 400 μm for particle diameters of 6.86, 8.34, 9.78, and 11.93 μm, respectively. The screening length of the interaction varied with

particle size because the different mass particles levitated at different heights above the lower electrode with different plasma properties.

B. Corrections for non-nearest-neighbor interactions

In the full ''molecular-dynamics'' simulations of the dust particle motion and crystallization, we include the pair interaction summed over all dust particles. However, in the equation-of-state analysis, only the NN interactions were included because of the short range of the exponentially shielded Debye interaction in the ordered array. In the study of finite 2D lattices [6], a correction to the NN approximation was found which improved the simple EOS analysis. We can make an approximate correction for non-NN effects by the following.

Consider a single particle in a uniform 1D line. There are two NN particles at distance s. The next-NN group has two particles at distance $2s$, then two more at $3s$, and so on. This total interaction energy, per particle, is given by the sum

$$V_{\rm eff}(s)=V_{pair}(s)+V_{pair}(2s)+V_{pair}(3s)+\cdots, \quad (14)$$

which for the Yukawa or Debye form of the pair potential is easily summed to give

$$V_{pair}^{Debye}(s)=A\frac{1}{s}\exp(-s/\lambda),$$

$$V_{\rm eff}(s)=A\frac{1}{s}\ln\left(\frac{1}{1-\exp(-s/\lambda)}\right). \quad (15)$$

An examination of the sum shows that the non-NN correction is relatively less important for the linear array than the 2D disk of dust particles. For our conditions, a typical non-NN interaction length of $s/\lambda=3$ yields $V_{pair}^{Debye}(s)/V_{\rm eff}(s)=0.97$. For this reason and algebraic simplicity, we do not include it in the regression analysis to determine Z and λ.

C. Atomistic force balance

Due to the relatively small number of particles present in the linear arrangements, it is straightforward to write a set of coupled equations to describe the particle positions in terms of Z and λ. We take the repulsive force f_r as a screened Coulomb interaction, as shown in Eqs. (6) and (10), and the radial dependent force term due to gravity f_w as given by Eq. (1). Considering a line of 11 particles as an example, the force balance equation for the particles, assuming symmetry about the center of the line and including both nearest and second nearest neighbors, can be written as a set of coupled equations,

$$f_r(r_{45})+f_r(r_{35})=f_w(r_5),$$

$$f_r(r_{34})+f_r(r_{24})=f_w(r_4)+f_r(r_{45}),$$

$$f_r(r_{23})+f_r(r_{13})=f_w(r_3)+f_r(r_{34})+f_r(r_{35}),$$

$$f_r(r_{12})+f_r(r_2)=f_w(r_2)+f_r(r_{23})+f_r(r_{24}),$$

$$f_{rf}(r_1)+f_r(2r_1)=f_w(r_1)+f_r(r_{12})+f_r(r_{13}), \quad (16)$$

where r_{ij} is the spacing between the two particles denoted as i and j, and r_k is the spacing between the kth point and the center of line, with the particles labeled from 1 to 5 from the center to the edge. For this set of equations, non-nearest-neighbor interactions are included and are represented by the radial index terms that have a difference of 2. Similar sets of coupled equations can be written for two or more particles confined to a linear potential well. Using Z and λ as regression parameters and the difference between measured and calculated positions for all lines of two to twelve particles as an error measure, we optimize Z and λ to produce the best fit to *all* of the particle positions.

Particle positions for one to twelve particles are shown in Fig. 4 for four different particle diameters. The data were obtained by putting a fixed number of particles in the line, photographing the particle positions, then using our image-processing algorithms to extract particle locations. We then change the number of particles and take a new photograph. The zero-particle position is determined from the center of mass for each particle line and varied by less than 0.05 mm for all particle lines. The positions of particles not at the center were averaged with the symmetrically located particle position and the positions were plotted from a radial position of zero outward. The lines connect the particle positions calculated from the optimum Z and λ. Values for Z and λ are shown in each graph. In general, the calculated positions appear to be in good agreement with measured values. Displacing the particles 5% from their measured positions, as could be produced by random thermal variations, tested the sensitivity of the fit to small variations in the particle positions. The optimum Z and λ values that fit the displaced arrangements were approximately 10% different from those determined from the undisplaced experimental data.

For our experimental conditions, the force due to non-nearest-neighbors can be characterized as small but not quite negligible. By way of example, we consider a typical screening length of 300 μm, a typical interparticle spacing of 0.5 mm, and a screened Coulomb interaction. The ratio of the repulsive force due to second nearest neighbors to nearest neighbors is 10%. For our conditions, we can safely neglect third-nearest-neighbor interactions since that force ratio is 1.4%. Due to the relative simplicity of the force balance equations in Eq. (16), we can turn off the non-nearest-neighbor interactions and observe the effect on the optimum Z, λ, and calculated positions (Fig. 5). The optimum Z and λ vary by approximately 15%; however, to the eye the calculated positions based upon the fit Z and λ look very close. Thus it would be easy to be misled by the apparently good fit, even if all the important forces are not included.

The values for Z and λ obtained from the 1D EOS and the two global fit models are summarized in Fig. 6. In general, the values obtained using these three methods agree to within 20% and they have the same scaling with particle diameter. The uncertainty for the 1D EOS fits is shown as the error bars in the figure. Comparison of these values of Z and λ with our previous measurements and with other values in the literature are within a factor of 2 [5,6,21,22]. However, direct

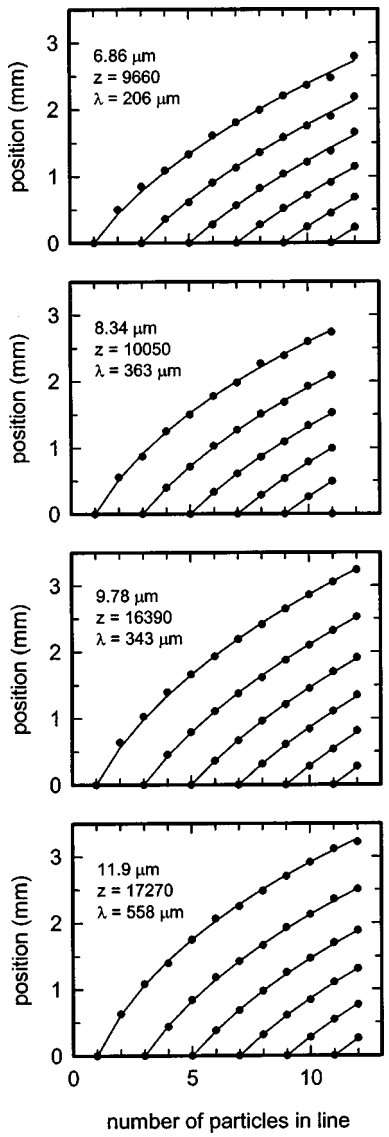

FIG. 4. Position of the particles as functions of the number of particles in the line for four different particle sizes. The points are measured values. The zero-particle position is determined from the center of mass for each particle line and varied by less than 0.05 mm for all particle lines. The positions of particles not at the center were averaged with the symmetrically located particle position and the positions were plotted from a radial position of zero outward. Thus it appears as if only half the line is plotted. The lines connect the particle positions calculated from the optimum Z and λ. Values for Z and λ are shown in each figure. The pressure was 100 mTorr.

comparison is complicated due the sensitivity of Z and λ to plasma conditions, gas, and in some cases confining geometry. We note that previous work showed good agreement between deriving Z and λ from a 2D EOS compression analysis and the particle oscillation technique [6].

IV. WAKEFIELD POTENTIAL

Due to the charge on the particles, they levitate in a region of the rf sheath where the time-average electric field is approximately 5–20 V/cm [6]. Because the particles are relatively massive compared with ions and electrons, their position is fixed while the electrons and ions sweep past them on rf time scales. An ion-induced-wakefield potential is formed on the downstream side of the negatively charged particles as the positive ions flow past, and are focused by the negatively charged particles. The electron behavior is more thermal

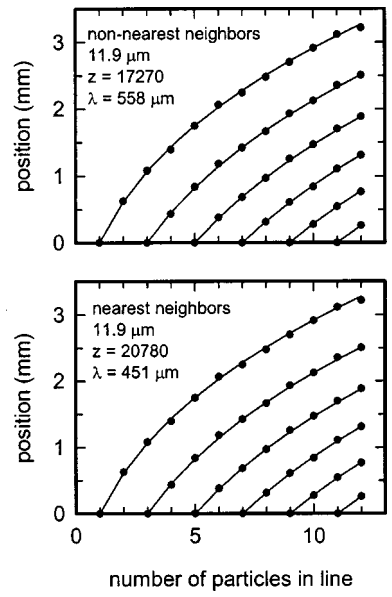

FIG. 5. The lines connect calculated particle positions assuming non-nearest-neighbor interactions and only nearest-neighbor interactions. Fit values for Z and λ are shown in each figure. The data points are for the 11.9 μm particles shown in Fig. 4.

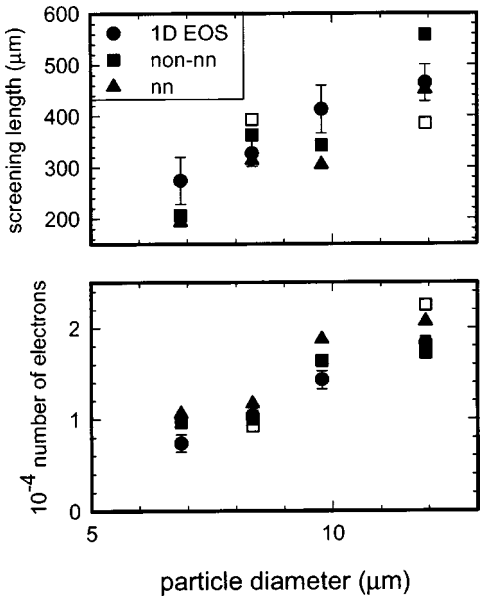

FIG. 6. Charge on the particle Z and screening length λ as functions of the particle diameter. The values were derived using three different methods, the 1D equation of state (1D EOS), and the full particle interaction model including non-nearest neighbors (non-nn) and only nearest neighbors (nn). The solid points were for a pressure of 100 mTorr while the open symbols were for 60 mTorr (only determined using the non-nn model).

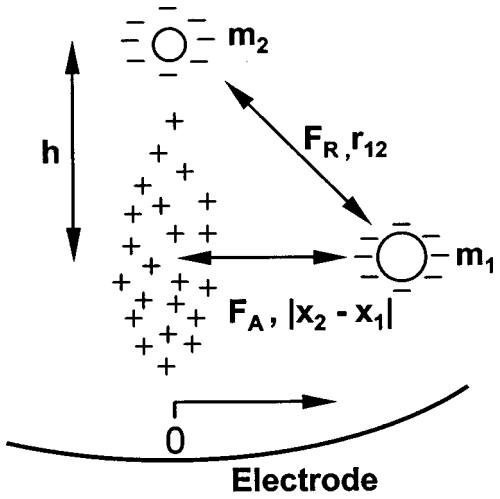

FIG. 7. Schematic of two particles showing upper particle of mass m_2, lower particle of mass m_1, and ion wakefield (positive space-charge region) below the upper particle. The 0.5 m radius of curvature of the lower electrode is greatly exaggerated. The height difference between the particles was h and the interparticle separation was r_{12}. The center of the well is defined as zero and the horizontal distance of the particles from the center of the well is x_1 or x_2.

(collisional) and they act to shield the ion space charge. The structure of the ion wakefield has been calculated by several groups, each using various simplifying assumptions for this computationally challenging problem [1,4,17,24,25]. Under certain conditions, the resulting positive space-charge region can produce relatively strong attractive electrostatic interactions with other particles. However, we note that even the basic idea of electrostatic attraction is open to discussion [26]. A schematic of the simplified particle interaction is shown in Fig. 7. The upper particle of mass m_2 has a smaller diameter and mass than the lower particle of mass m_1. Considering only dominant interactions, the upper particle interacts with the lower particle via repulsive interactions arising from the screened Coulomb potentials as characterized by each particle's Z and some λ appropriate for the pair. However, the lower particle also reacts to an electrostatic attractive interaction between the positive space-charge region and the negative dust particle's surface charge, in addition to the reciprocal repulsive interactions with the upper particle. While there is also a space-charge region below the lower particle, for our conditions, we estimate that it does not strongly interact with the negative charge of the upper particle due to its relatively large distance and thus we do not include it in our force analysis.

Collisions between two particles at unequal heights are used to measure the ion wakefield potential. An example of a time-dependent trajectory is shown in Fig. 8 for one 8.3-μm-diam particle interacting with one 11.9-μm-diam particle. Only the horizontal distance between the particles is shown or analyzed. The vertical distance between the particles varied by less than 0.02 mm, reflecting the strong vertical confining forces and the lack of changes in the particle charge. For this particular set of particles, the top particle was added first, then came a rest at a horizontal position of zero (not

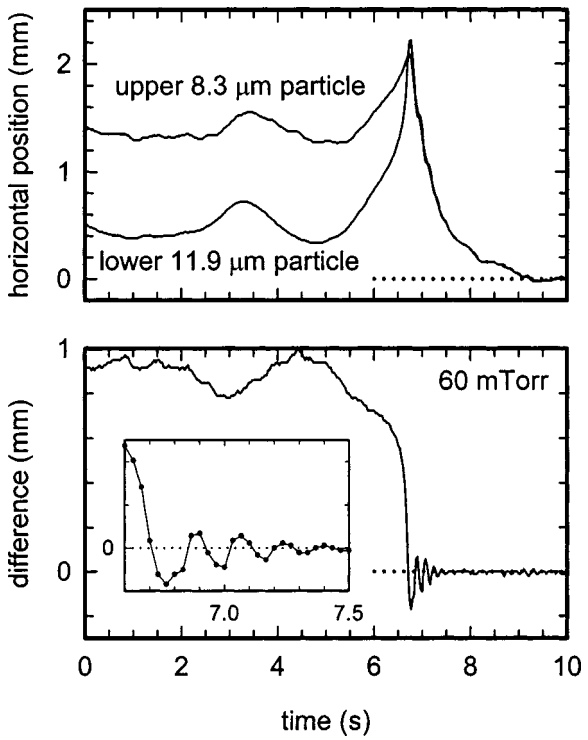

FIG. 8. Horizontal (x) coordinates of the 8.34- and 11.93-μm-diam particles as a function of time at 60 mTorr. The upper plot shows the time-dependent particle positions relative to the center of the well while the lower plot shows the difference between the two positions. The inset in the lower plot is an expanded view of the particle oscillation.

shown in this figure). At later time, the lower particle was added and both the upper and lower particle came to a new quasiequilibrium position *offset* from the bottom of the gravitational potential well ($r=0$). This offset behavior was previously observed in both this geometry and other work [16,17]. In those cases, the off-axis position was likewise stable.

The nonvertically aligned pairs show correlated motion and the importance of random thermal velocity in the relatively slow rate of vertically aligned pair formation. At $t \approx 3.5$ s, the lower particle moves towards the upper particle (due to relatively large thermal motions) and the upper particle moves away and up the gravitational well. The lower particle then retreats and the upper particle moves back down the well. In this case, the upper particle motion is driven by the lower, which is not the case when the particles form a vertically aligned pair. At $t \approx 6$ s, the random thermal motion of the lower particle is large enough to overcome the repulsive potential and the lower particle falls into the attractive potential, forming a vertically aligned pair. For this set of conditions, the horizontal oscillations of the lower particle in the bottom of the potential well are relatively large [17]. While the data are noisy, the averaged horizontal oscillations from several experiments have a dominant frequency of approximately 3 Hz. The 3 Hz oscillation does not change significantly with time, indicating that the bottom of the attractive potential is quasiparabolic. After the vertical pair is formed, the horizontal force was removed and the pair drifts

back to $r=0$ with a single exponential decay whose time constant is given by the drag on the *upper* particle. In contrast with the nonvertically aligned pairs, the lower particle in the aligned pair follows the upper particle position since it is trapped in the ion-wakefield-potential well. In all cases, there was a delay time of 1–10 s between the formation of an off-axis, nonaligned pair and the rapid formation of a vertically aligned pair. This difference is attributed to the importance of random thermal energy (Brownian motion) providing an extra velocity kick to the lower particle to overcome a repulsive potential energy barrier before falling into the attractive wakefield potential. The ability to observe a macroscopic process controlled by stochastic molecular events (Brownian motion) seems rather unique in kinetics. It is in fact a prototypical model of a chemical reaction.

The interaction potentials are obtained from the particles' position and velocity by numerically inverting the NEOM (Newtonian equations of motion) shown below. Due to the experimental geometry and vertically constrained motion, we have only a 1D set of equations. The upper particle interacts with the lower particle through a repulsive potential $V_D(r_{12})$, where $r_{12}=\sqrt{(x_1-x_2)^2+h^2}$, with h the vertical spacing between the particles and x_i the Cartesian coordinate parallel to the trough (Fig. 7). The lower particle, however, responds to both the above repulsive interaction and an attractive force generated between it and the wakefield, $V_A(|x_1-x_2|,h)$. In this limit, the NEOM for the two particles are

$$m_1\ddot{x}_1+m_1\gamma_1\dot{x}_1+k_1x_1=\left(\frac{x_2-x_1}{r_{12}}V_D'-\frac{\partial}{\partial x_1}V_A(|x_1-x_2|,h)\right), \tag{17}$$

$$m_2\ddot{x}_2+m_2\gamma_2\dot{x}_2+k_2x_2=\frac{x_1-x_2}{r_{12}}V_D'(r_{12}), \tag{18}$$

where m_i is the mass, γ_i is the Epstein drag coefficient, and $k_i=m_ig/R_c$ with g the acceleration due to gravity and R_c the radius of curvature of the electrode. The subscript 1 denotes the lower particle and the subscript 2 denotes the upper particle. Solving for $f_A=-(\partial/\partial x_1)V_A(|x_1-x_2|,h)$ and the repulsive force $f_R=V_D'(r_{12})$ as functions of the interparticle spacing yields

$$f_A=m_1\ddot{x}_1+m_1\gamma_1\dot{x}_1+k_1x_1+m_2\ddot{x}_2+m_2\gamma_2\dot{x}_2+k_2x_2, \tag{19}$$

$$f_R=\frac{r_{12}}{x_1-x_2}[m_2\ddot{x}_2+m_2\gamma_2\dot{x}_2+k_2x_2]. \tag{20}$$

Thus the attractive and repulsive potentials can be derived from only the particle positions as functions of time. The first and second derivatives (velocity and acceleration) were calculated after three-point smoothing was performed on the time-dependent position data. Experimentally measured Epstein gas-damping rates (100 mTorr) of 30, 25, 22, and 17.5 s^{-1} were used for the 6.86-, 8.34-, 9.78-, and 11.93-μm-diam particles, respectively. Rather than use calculated Epstein drag coefficients, we experimentally determine the values for each experimental condition, since we find that the value of the attractive force, which should be zero for large particle separations, depended strongly on the value of the gas drag. As in previous work, the measured drag coefficients are in good agreement with calculated values to within the uncertainty introduced by the dominate neutral scattering mechanism and gas temperature [6,27]. We note that our novel technique of directly inverting the NEOM avoids specifying the functional forms of the particle-particle interaction. As the lower particle moves into the space charge region, it will change the shape of the ion wakefield potential. Because we know the confining force due to the curved electrode, the drag force due to neutral gas scattering, and the charges of the particles by single-layer analysis [5,6], we can isolate the *full* interaction of the particles. The ion wakefield potential can be obtained by integrating the force maps discussed below.

Experimentally determined attractive potentials are shown in Fig. 9 as functions of the horizontal particle separation $|x_2-x_1|$, pressure [graphs (a) and (b)], and vertical particle spacing [graphs (c) and (d)]. Data from three to eight collision events are shown. Whether an upper particle was injected towards the already present lower particle or vice versa made no difference, as previously observed. For these experimental conditions, the peak attractive force varied between 230 and 60 fN with a maximum force obtained at horizontal particle separations between 200 and 300 μm. Decreasing the pressure from 100 to 60 mTorr resulted in an increase in the peak attractive force from 160 to 230 fN as well as a slight broadening of the potential. The increase may be due to several possible mechanisms. Decreasing the pressure would increase the ion mean free path and the magnitude of the ion focusing below the upper particle. A higher positive ion space charge would result in a stronger attractive potential. In addition, the lower pressure also results in less gas drag, which can increase the peak velocity and force. Measurements of the charge and screening length discussed above and shown in Fig. 6 do not vary greatly with pressure, so changes due to particle properties are likely secondary. Increasing the lower-particle diameter from 9.8 to 11.9 μm increased the vertical particle separation from 0.55 to 0.75 mm and decreased the peak attractive force from 110 to 60 fN. Due to different mass, the 11.9 μm particle integrates a different horizontal slice of the ion wakefield potential than the 9.8 μm particle. Despite the larger charge on the 11.9 μm particle, the peak attractive force was almost a factor of 2 smaller, likely due to the larger vertical particle separation. Thus the ion wakefield potential has a finite extent and decays fairly rapidly with vertical distance below the upper particle. These observations are consistent with most models of the wakefield potential [1,4,17,24,25].

Experimentally determined repulsive potentials are shown in Fig. 10 as functions of the absolute particle separation r_{12}, pressure [graphs (a) and (b)], and vertical particle spacing [graphs (c) and (d)]. Due to the (x_2-x_1) term in the denominator of Eq. (20), the repulsive data became very noisy as the particles vertically pair and are not shown. Decreasing the pressure from 100 to 60 mTorr resulted in a slightly increased repulsive force. Since the charge on the particles and the screening length did not change greatly, one would not

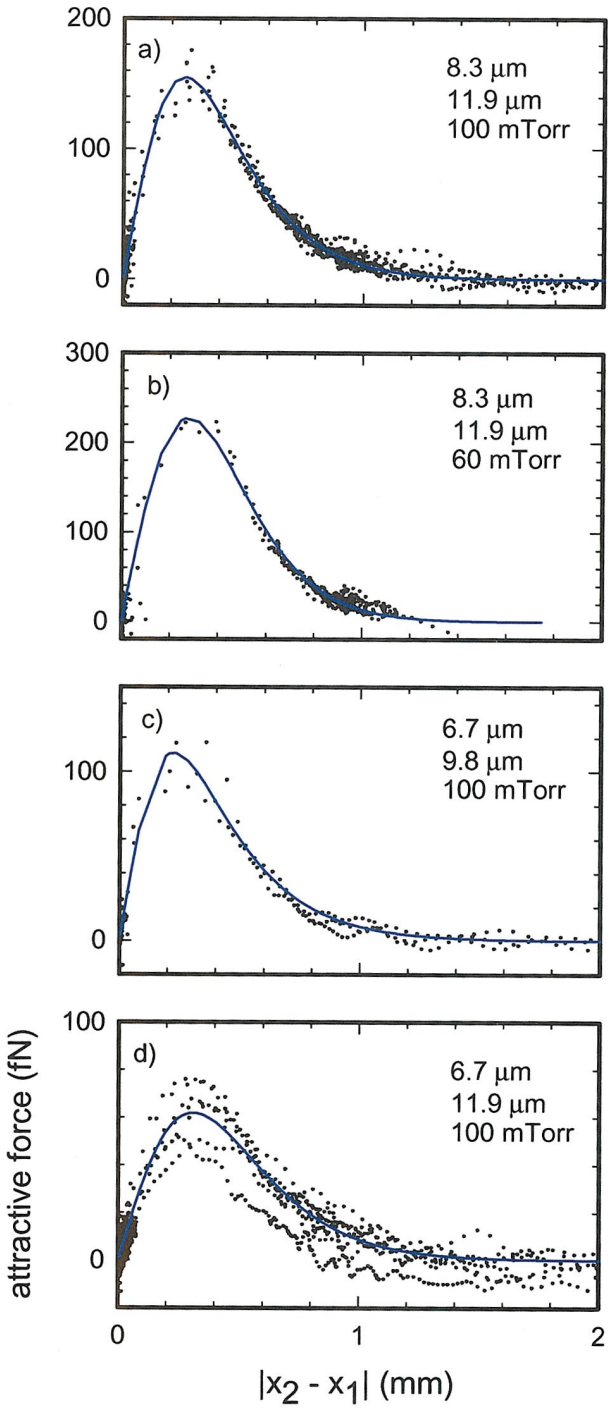

FIG. 9. (Color) Ion wakefield attractive potentials as functions of the horizontal interparticle spacing. The particle diameter and the pressure are shown in each plot. The data points are shown as points while the lines are fits to the attractive potential form described by Eq. (21). The fit parameters are in Table I.

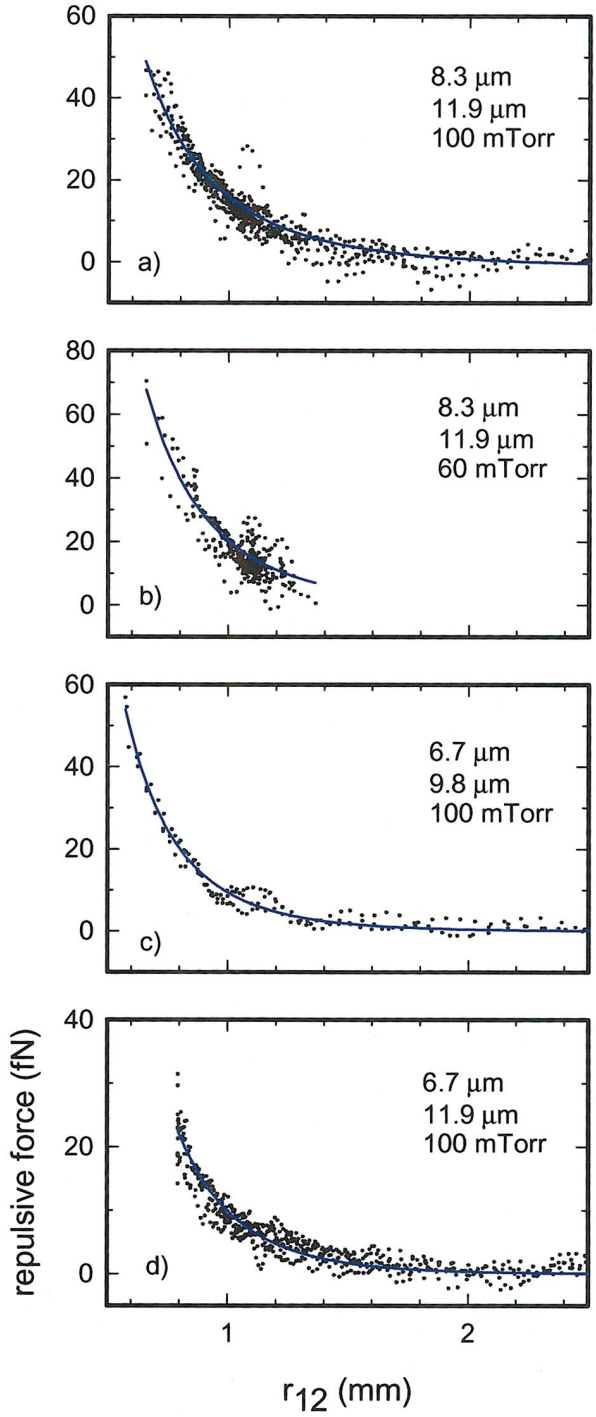

FIG. 10. (Color) Ion wakefield repulsive potentials as functions of the interparticle spacing. The particle diameter and the pressure are shown in each figure. The data points are shown as points while the lines are fits to a screened Coulomb potential described by Eqs. (6) and (10). The fit parameters are in Table II.

expect large changes in the repulsive potential. In addition, increasing the particle spacing by changing the particle mass resulted in small changes as well since the particle charge and screening length increased a small amount (to within the uncertainty).

The solid lines shown in Figs. 9 and 10 are regression fits to functional forms for the attractive and repulsive potential. The repulsive potential was fit to a screened Coulomb form [Eqs. (6) and (10)]. To find a functional form of the wakefield potential, we used an approximate thermal average of the first-order result for ion scattering from a Debye interaction of screening length λ_D [17]. That analysis showed that the dominant cylindrical radial dependence of the wakefield potential was

TABLE I. Values for regression fits to the attractive potential given by Eq. (21).

Particle diameter (μm)	Pressure (mTorr)	A_W/λ (10^{-14} N)	a (μm)	λ (μm)
8.3, 11.9	100	−397	410	185
8.3, 11.9	60	−5900	600	141
6.7, 9.8	100	−90	282	220
6.7, 11.9	100	−290	550	201

TABLE II. Values for regression fits to the repulsive potential given by Eq. (10).

Particle diameter (μm)	Pressure (mTorr)	A (10–20 Jm)	λ (μm)
8.3, 11.9	100	2.7	750
8.3, 11.9	60	4.3	557
6.7, 9.8	100	2.9	428
6.7, 11.9	100	3.5	390

$$V(r) = A_W \exp(-\sqrt{a^2 + r^2}/\lambda), \tag{21}$$

where A_W is a function of plasma and dust parameters, and a depends on the thermal averaging of ion motion. The usefulness of Eq. (21) lies in the fit to the experimental data; the approximations made in the derivation are too many to be universally useful as a predictive result. In general, the fits for both the attractive and repulsive potentials are good. Values for the attractive and repulsive fit parameters are shown in Tables I and II. From the regression fits we calculate that the wakefield potential well [Fig. 9(a)], if electrostatic, is about 0.2 V deep at the separation of the two particles of 0.6 mm, in reasonable agreement with our calculations [17]. The fit to the repulsive force yields an A_W value that is consistent with our measured particle charge but a λ that is approximately a factor of 2 larger than that derived from an analysis of the particle monolayer compression [6]. The larger value of the screening length is approaching the electron Debye length. We hypothesize that this is due to the higher ion velocity in the vicinity of the particles, giving less ion screening and a larger Debye length. However, the use of a single screening length to describe the repulsive interaction between two particles with unequal screening lengths is not physical and needs to be modified in future work.

V. SUMMARY

Plasma dust particle interaction potentials, charges Z, and screening lengths λ were derived from compressional and collisional measurements of the particle interactions in a simplified geometry. A slot in the mildly parabolic lower rf-driven electrode formed a narrow electrostatic trench that confined the particles to a line. This geometry was used for two different but complementary experiments. The first used particles of the same mass, and hence the same height above the lower electrode, and derived Z and λ from an analysis of the radially dependent particle spacing. Z and λ increased with increasing particle diameter. The slight parabolic curvature of the lower electrode gives rise to a radially dependent component of the gravitational force and radially dependent particle compression. Due to the relative simplicity of the geometry, a direct comparison could be made between a 1D equation-of-state analysis and an atomistic force balance approach. It was also possible to examine the effect of including or not including non-NN interactions. We found differences in the optimum Z and λ obtained from each technique were on the order of the ratio of nearest-neighbor to nonnearest-neighbor force. For this work, that difference was 10%.

The second set of experiments measured the ion wakefield force field generated by an upper lighter target dust particle by colliding it with a heavier probe dust particle levitated at a lower height. Attractive and repulsive interactions between charged particles were calculated using Newton's equations for a number of experimental conditions. This method does not assume a form for the interaction potential. The magnitude and structure of the attractive ion wakefield potential below a negatively charged dust particle levitated in the plasma sheath region were measured as a function of the pressure and interparticle spacing. The peak attraction was 230 fN while the peak repulsion was 60 fN. Peak attractive potential increased with lower pressure, likely due to an increased ion mean free path and hence increased positive ion space charge, and a decrease in the particle gas drag. In addition, the attractive potential has a finite vertical extent that decays fairly rapidly with vertical distance below the upper particle. Fits to the attractive force are in good agreement with our derived functional form while the repulsive forces are in good agreement with the classic screened Coulomb potential.

For some particle combinations, the influence of random thermal particle motion on the force balance is important. The energy provided by thermal motions was observed as correlated motion between nonvertically paired particles and provides the added energy (velocity) for the lower particle to overcome a small repulsive potential well and fall into the attractive potential.

ACKNOWLEDGMENTS

This work was supported by the Division of Material Sciences, BES, Office of Science, U.S. Department of Energy and Sandia National Laboratories, a multiprogram laboratory operated by Sandia Corporation, a Lockheed Martin Company for the U.S. Department of Energy's National Nuclear Security Administration under Contract No. DE-AC04-94AL85000.

[1] V. A. Schweigert *et al.*, Phys. Rev. E **54**, 4155 (1996).
[2] A. Melzer, V. A. Schweigert, I. V. Schweigert, A. Homann, S. Peters, and A. Piel, Phys. Rev. E **54**, R46 (1996).
[3] V. N. Tsytovich, Phys. Usp. **40**, 53 (1997).
[4] M. Lampe *et al.*, Phys. Plasmas **7**, 3851 (2000).
[5] G. A. Hebner *et al.*, Phys. Rev. Lett. **87**, 235001-1 (2001).
[6] G. A. Hebner, M. E. Riley, and K. E. Greenberg, Phys. Rev. E **66**, 046407 (2002).
[7] G. A. Hebner *et al.*, IEEE Trans. Plasma Sci. **30**, 94 (2002).
[8] U. Konopka, G. E. Morfill, and L. Ratke, Phys. Rev. Lett. **84**, 891 (2000).
[9] K. Takahashi *et al.*, Phys. Rev. E **58**, 7805 (1998).
[10] J. B. Pieper, J. Goree, and R. A. Quinn, Phys. Rev. E **54**, 5636 (1996).
[11] Y. Hayashi, Phys. Rev. Lett. **83**, 4764 (1999).
[12] G. E. Morfill *et al.*, Phys. Rev. Lett. **83**, 1598 (1999).
[13] V. Steinberg *et al.*, Phys. Rev. Lett. **86**, 4540 (2001).
[14] M. Zuzic *et al.*, Phys. Rev. Lett. **85**, 4064 (2000).
[15] A. Melzer, V. A. Schweigert, and A. Piel, Phys. Rev. Lett. **83**, 3194 (1999).
[16] A. Melzer, V. A. Schweigert, and A. Piel, Phys. Scr. **61**, 494 (2000).
[17] G. A. Hebner, M. E. Riley, and B. M. Marder, Phys. Rev. E **68**, 016403 (2003).
[18] D. A. Law *et al.*, Phys. Rev. Lett. **80**, 4189 (1998).
[19] D. Samsonov *et al.*, Phys. Rev. Lett. **83**, 3649 (1999).
[20] A. Homann *et al.*, Phys. Rev. E **56**, 7138 (1997).
[21] A. Homann, A. Melzer, and A. Piel, Phys. Rev. E **59**, R3835 (1999).
[22] E. B. Tomme *et al.*, Phys. Rev. Lett. **85**, 2518 (2000).
[23] P. J. Hargis, Jr. *et al.*, Rev. Sci. Instrum. **65**, 140 (1994).
[24] S. V. Vladimirov, S. A. Maiorov, and N. F. Cramer, Phys. Rev. E **67**, 016407 (2003).
[25] F. Melandso and J. Goree, Phys. Rev. E **52**, 5312 (1995).
[26] G. Lapenta, Phys. Rev. E **66**, 026409 (2002).
[27] P. S. Epstein, Phys. Rev. **23**, 710 (1924).